

Temperature-Triggered Supramolecular Assembly of Organic Semiconductors

Hongliang Chen, Weining Zhang, Shizhao Ren, Xingang Zhao, Yang Jiao, Yu Wang, J. Fraser Stoddart,* and Xuefeng Guo*

Dedicated to Professor Daoben Zhu on the occasion of his 80th birthday

Supramolecular assembly is a promising bottom-up approach for producing materials that behave as charge transporting components in electronic devices. Although extensive advances have been made during the past two decades, formidable challenges exist in controlling the local randomness present in supramolecular assemblies. Here, a temperature-triggered supramolecular assembly strategy using heat to heal defects and disorders is reported. The central concept of the molecular design—named the "Tetris strategy" in this research—is to: i) increase the rotational freedom of the molecules through thermal perturbation, ii) induce conformation-fitting of adjacent molecules through two different kinds of intermolecular $[\pi \cdots \pi]$ interactions, and finally iii) lock the nearby molecules in inactive co-conformations. Experimentally, upon heating to 57 °C, amorphous solid-state films undergo spontaneous assembly, leading to the growth of uniform and highly ordered microwire arrays. Temperature-triggered supramolecular assembly provides an approach closer to the precision control of assembled structures and presents with a broad canvas to work on in approaching a new generation of supramolecular electronics. Tetris is a registered trademark of Tetris Holding, LLC, used with permission.

by Schenning and Meijer.^[11,14] Supramolecular electronics relies on the bottom-up construction of hierarchical assemblies through a combination of weak noncovalent bonding interactions—i.e., van der Waals,^[15] hydrogen^[16–18] and halogen^[19–21] bonding, amphiphilic interactions,^[22–25] $[\pi \cdots \pi]$ stacking,^[2,5] Coulombic^[26,27] and charge transfer interactions.^[28–30] During the past two decades, significant progress^[2,5,9,10,12,13] has been made in the construction of supramolecular assemblies with specific architectures and morphologies, such as helical dendrimers,^[31] gels,^[32–35] nanoribbons,^[36–38] nanotubes,^[22,39,40] nanowires,^[41] heterojunctions,^[42–44] monolayers,^[45–47] and 2D crystals.^[48–53] Generally, highly ordered supramolecular architectures and networks with few defects are favorable for achieving desirable electrical properties.^[54–57]

Even after considering the appreciable returns from various architectures and networks, one major challenge, when carrying out supramolecular assemblies, remains controlling local randomness at different hierarchical levels of the superstructure. On account of the spontaneous nature and rapidity associated with supramolecular assembly processes, it is difficult to avoid local defects and disorders in the resulting superstructures. These imperfections often lead to an impairment in electrical properties. Recent theoretical advances reveal^[58–60] that defects are an intrinsic part of supramolecular polymers and soft self-assembled systems when inherent dynamics govern their assembly.

1. Introduction

Bottom-up self-assembly^[1–4] is considered these days by many scientists^[5–9] to be a promising approach to the construction of materials for the semiconductor industry. The approach^[6,7,9] is ecofriendly, morphologically and functionally flexible, and facilitates easy and cost-effective device fabrication. Efforts to integrate nano-/microstructures as charge transporting components in electronic devices have led to the emergence of supramolecular electronics,^[5,10–13] which was conceptualized in the beginning

of the spontaneous nature and rapidity associated with supramolecular assembly processes, it is difficult to avoid local defects and disorders in the resulting superstructures. These imperfections often lead to an impairment in electrical properties. Recent theoretical advances reveal^[58–60] that defects are an intrinsic part of supramolecular polymers and soft self-assembled systems when inherent dynamics govern their assembly.

Dr. H. Chen, Dr. X. Zhao, Dr. Y. Jiao, Dr. Y. Wang, Prof. J. F. Stoddart
Department of Chemistry
Northwestern University
Evanston, IL 60208, USA
E-mail: stoddart@northwestern.edu

Dr. H. Chen, Prof. J. F. Stoddart
Stoddart Institute of Molecular Science
Department of Chemistry
Zhejiang University
Hangzhou 310027, China

 The ORCID identification number(s) for the author(s) of this article can be found under <https://doi.org/10.1002/adma.202101487>.

Dr. H. Chen, Prof. J. F. Stoddart
ZJU-Hangzhou Global Scientific and Technological Innovation Center
Hangzhou 311215, China

Dr. W. Zhang, Dr. S. Ren, Prof. X. Guo
Beijing National Laboratory for Molecular Sciences (BNLMS)
State Key Laboratory for Structural Chemistry of Unstable and Stable Species
College of Chemistry and Molecular Engineering
Peking University
Beijing 100871, China
E-mail: guoxf@pku.edu.cn

Prof. J. F. Stoddart
School of Chemistry
University of New South Wales
Sydney, NSW 2052, Australia

DOI: 10.1002/adma.202101487

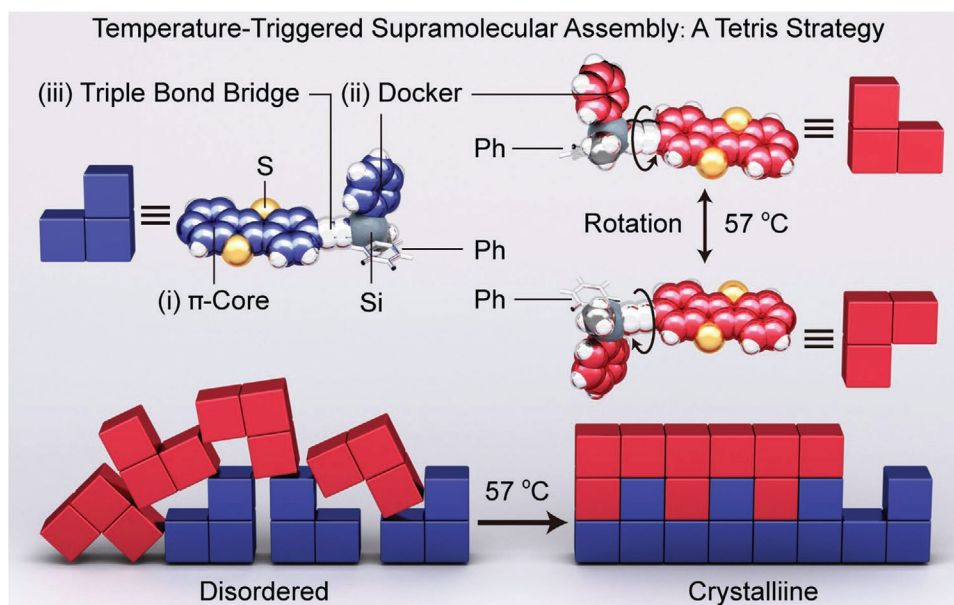


Figure 1. Schematic illustration showing the temperature-triggered supramolecular assembly explained using the Tetris strategy as an analogy. Tetris is a registered trademark of Tetris Holding, LLC, used with permission.

In an attempt to control precisely the relative orientations of molecules during supramolecular assembly processes and thus obtain highly ordered superstructures, one solution is to harness^[22,39,42] multiple, synergistic noncovalent bonding interactions. Another solution, however, is to retain^[61] the dynamics associated with noncovalent bonding interactions so as to attain fine tuning of molecular packing through external control—i.e., chemical initiators,^[62–64] light,^[65–69] or temperature^[70]—to trigger^[71] self-assembly for better control over uniformity and dispersity at the supramolecular level. Here, we propose (Figure 1) a molecular design strategy in order to achieve a temperature-triggered supramolecular assembly of organic semiconductors (OSCs) in solid-state films. The molecules in Figure 1 (top left) are composed of three parts—namely, i) a conjugated π -core and ii) a diphenylsilyl docker, bridged through iii) a carbon–carbon triple bond. The central structural feature of this design is that the diphenylsilyl docker can rotate around the axis defined by the triple bond (Figure 1, top right) upon heating, leading to: i) a change in the orientation of the diphenylsilyl dockers, ii) the fitting of the colored (red and blue) phenyl rings to the conformations of neighboring molecules, iii) thus forming a dimer as a result of the $[\pi \cdots \pi]$ interactions between the diphenylsilyl dockers, and finally iv) growing into long-range ordered superstructures. This approach can be compared to playing (Figure 1, bottom) the Tetris game—that is, the molecule can be treated as J- or L-shaped building blocks. The Tetris game allows changing the orientation the blocks—, e.g., from L to Γ —in order to control molecular packing accurately and achieve a well-organized arrangement of building blocks.

The compound—referred to (see Figure 2a) as T-C₁₀—consists of a conjugated benzothieno[3,2-b]benzothiophene^[72–77] (BTBT) backbone as the π -core and a decyl chain^[72,78,79] (C₁₀) as a σ -substituent on the right-hand side of the π -core. A diphenylmethylsilyl docker was introduced onto the left-hand side of the π -core with a carbon–carbon triple bond forming a bridge. Thin

films were prepared by spin-coating a CHCl₃ solution of T-C₁₀ onto silicon substrates (Figure 2b). After heating at 57 °C ($T < T_{\text{melt}}$), the amorphous film crystallized to afford ultralong, high-density, and highly ordered microwire arrays (Figure 2c and Figure S29, Supporting Information), resulting from the temperature-triggered supramolecular assembly in the solid state. In order to verify the experimental results, we synthesized three more control compounds (Figure 2a)—namely C-1, C-2, and C-3. C-1 and its many derivatives^[72,80,81] are classic liquid-crystalline OSCs. C-2 with a trimethylsilyl substituent is also more liquid-crystalline-like because the trimethylsilyl group is much smaller, with no noncovalent bonding interactions to tune the packing of the π -cores. For C-3, however, the thermal behavior is more complicated than that observed for T-C₁₀ because the bridge between the diphenylmethylsilyl docker and the π -core is a carbon–carbon single bond, which is more flexible than the carbon–carbon triple bond in T-C₁₀. This structural feature offers more degrees of freedom, allowing the docker to rotate during the heating process, creating numerous conformations, a situation that is detrimental to crystallization. We performed detailed thermal and structural characterizations of these compounds and measured their field-effect transistor properties in a bottom-gated top-contact device configuration in order to reveal any hidden structure–property relationships in this temperature-triggered supramolecular assembly mechanism.

2. Results and Discussion

2.1. Synthesis

The target compound T-C₁₀ was synthesized (Scheme S1, Supporting Information) using a Sonogashira reaction to couple an iodinated BTBT derivative (IBTBT-C₁₀) with ethynyl(methyl) diphenylsilane. The classical method (Scheme S1, Supporting

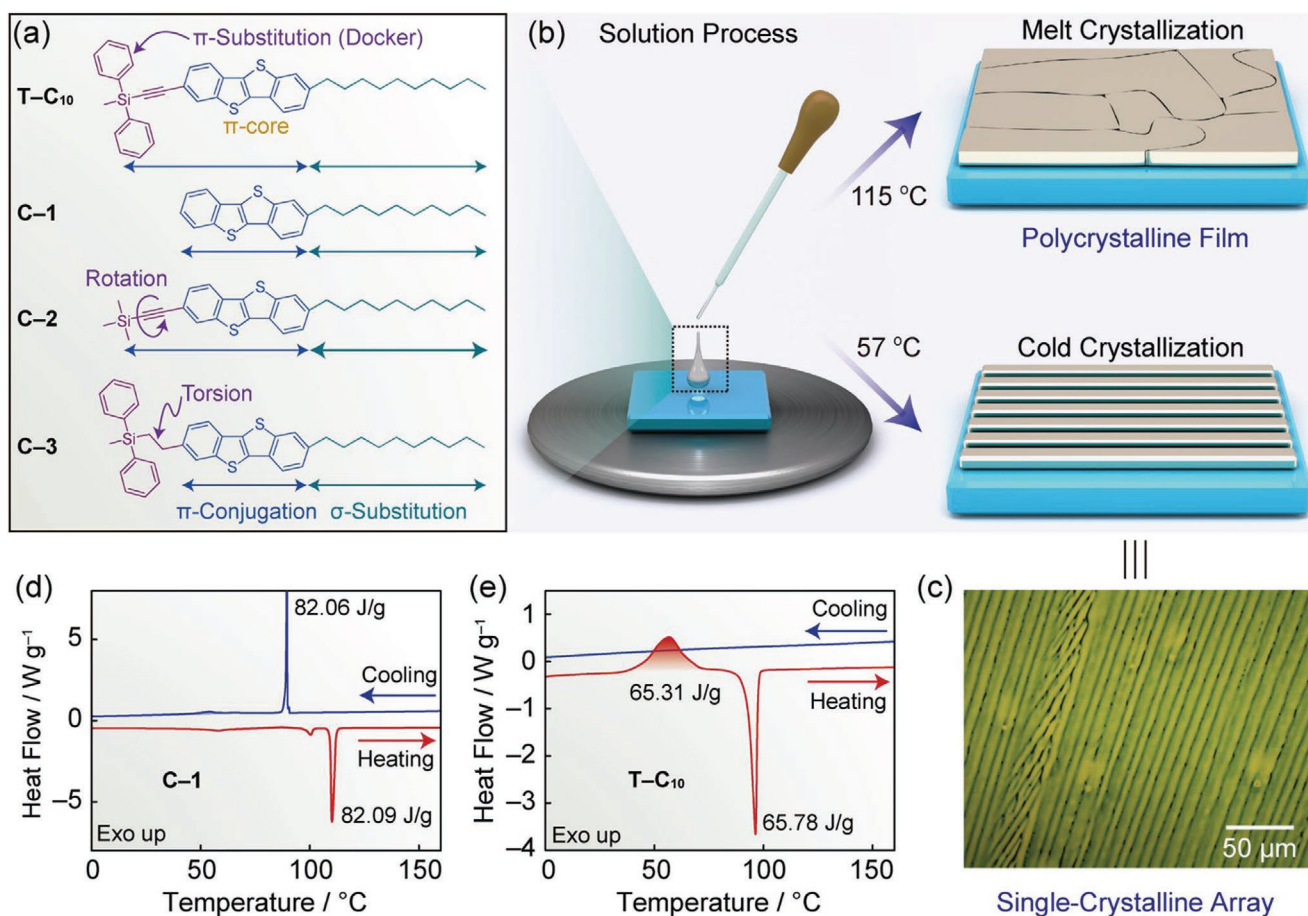


Figure 2. Formation of the single-crystalline organic semiconductor (OSC) arrays. a) Structural formulas of the target (T-C₁₀) and control (C-1, C-2, C-3) molecules. b) Schematic illustration showing the solution process used to fabricate the OSC films. The top right image portrays the melt crystallization—namely, the film of C-1 was heated above its melting point and crystallized during the cooling process, resulting in polycrystalline films. The bottom right portrays the cold crystallization—namely, the amorphous film of T-C₁₀ crystallized into single-crystalline wire arrays when the temperature reaches 57 °C during the heating process. c) Optical microscopy showing a high-density oriented microwire array of T-C₁₀ after cold crystallization. d,e) Differential scanning calorimetry (DSC) curves of C-1 (d) and T-C₁₀ (e) at a scanning rate of 5 K min⁻¹. There is an endothermic peak caused by cold crystallization in the heating cycle of T-C₁₀.

Information, Route I) of synthesizing IBTBT-C₁₀ leads to a low overall yield ($\approx 5\%$) for aromatic compounds because of their poor solubility in H₂O and the instability of some of the intermediates. In order to improve the synthetic efficiency, we adopted^[82] the aromatic Finkelstein reaction and iodinated the aromatic BTBT core (Scheme S1, Supporting Information, Route II). The overall yield of Route II increased dramatically to $\approx 53\%$, almost 10 times higher than the yield ($\approx 5\%$) obtained using Route I. Detailed synthetic protocols and characterizations of target and control compounds can be found in Section B, Schemes S1–S11, and Figures S1–S16 (Supporting Information).

2.2. Thermal Analysis of the Supramolecular Assembly Process

With the target and control compounds in hand, we started an investigation of their thermal properties. Thermogravimetric analysis (TGA) revealed (Figure S19, Supporting Information) a 5% weight loss at 385 °C, indicating the high stability of

T-C₁₀. In differential scanning calorimetry (DSC) experiments, the control compound C-1, with a rigid π -core and flexible σ -substitution, crystallized (Figure 2d) at ≈ 90 °C when cooling down from the melt state, exhibiting a phenomenon which is termed “melt crystallization.”^[72] In the case of T-C₁₀, however, an exothermic peak at ≈ 57 °C was present (Figure 2e) during heating, while no crystallization peak was observed on cooling. This phenomenon indicates that the temperature-triggered assembly is more like a “cold crystallization.”^[83] Crystallization is reproducible (Figure S20, Supporting Information) regardless of the number of heating cycles undergone. As expected, the thermal behavior of the control compound C-2 was more “melt crystallization”-like (Figure S21a, Supporting Information) because of the smaller size of the trimethylsilyl group. In the case of C-3, however, more endothermic peaks were observed (Figure S21b, Supporting Information) during the heating cycle, indicating that the self-assembly of C-3 is much more complicated than that observed in the case of T-C₁₀. This difference can be attributed to the flexible bridge between the bulky dockers and the π -core which offers more freedom for the

molecule to adjust its conformation upon heating. The DSC experiments demonstrate that the phenylene ring in the docker and the relatively rigid conformation of the molecule play important roles in the temperature-triggered assembly process.

2.3. Kinetics Investigation

In order to optimize the thermal conditions to trigger supramolecular assembly, we investigated (Figure 3) the influence of heating and cooling rates on the thermal response of T-C₁₀. If the material was treated with the same heating/cooling rate, the crystallization peak moved (Figure S22, Supporting Information) to higher temperatures with an increase in the scanning rates and disappeared when the scanning rate was faster than 20 K min⁻¹. The enthalpies of crystallization under different scanning rates varied and only remained stable

(Figure 3a) in a narrow range from 2 to 10 K min⁻¹ with an enthalpy change of 38.7 ± 1.3 kJ mol⁻¹. As a result, accurate control of the temperature windows and heating/cooling rate is essential. Next, we held (Figure S23a, Supporting Information) the heating rate at 10 K min⁻¹ in order to investigate the effect of the cooling rate. Although the crystallization peak did not appear (Figure S23b, Supporting Information) during the cooling process, we found (Figure S23a, Supporting Information) that the difference in cooling rates, i.e., changing from 2 to 50 K min⁻¹, caused a shift of the cold crystallization temperature to 6 degrees C higher. This observation can be attributed to the difference in relative crystallinity of the amorphous state obtained on slow cooling of the melt. In order to achieve the same relative crystallinity, we fixed (Figure 3b) the cooling rate at 10 K min⁻¹, while the heating rate was changed from 2 to 50 K min⁻¹. Since the crystallization peak moved (Figure 3b and Table S2, Supporting

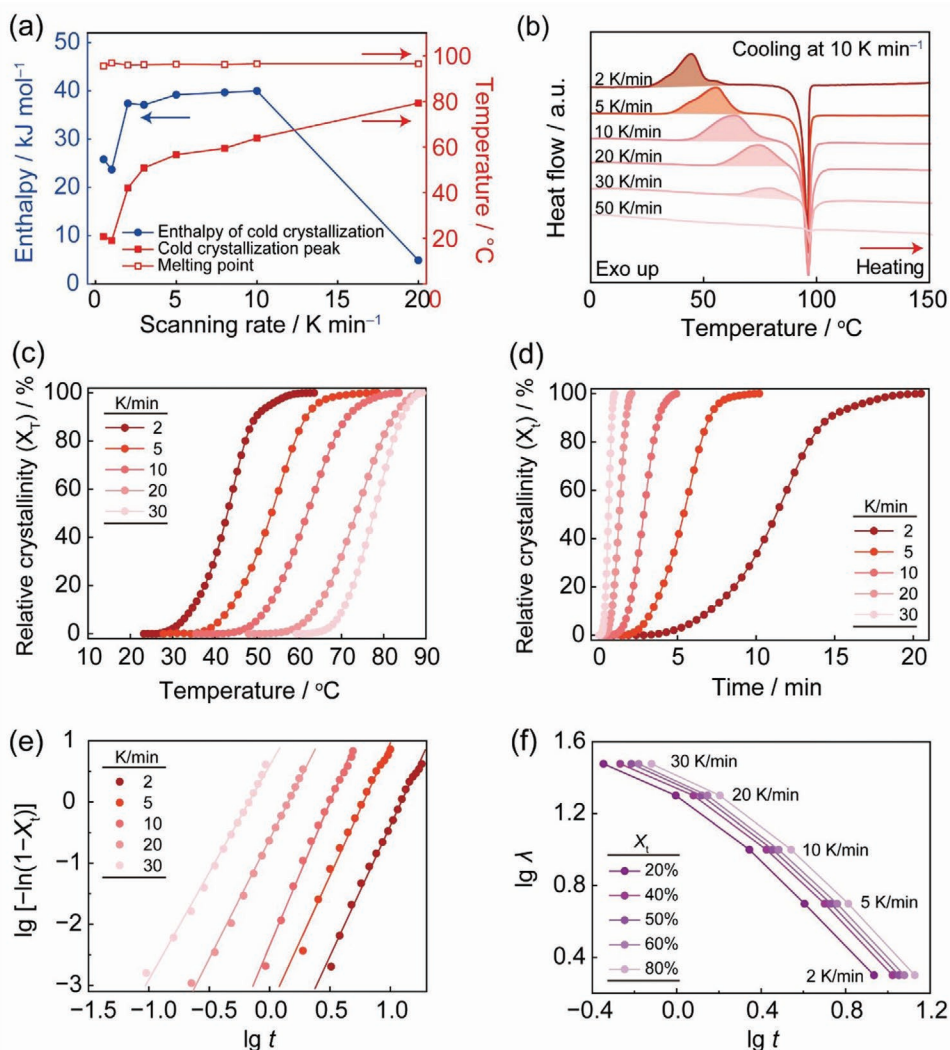


Figure 3. Thermal analysis of T-C₁₀. a) The melting point, cold crystallization temperature, and change in enthalpy at different scanning rates. b) DSC heating scans of T-C₁₀ at six different heating rates. The sample was cooled down at a fixed rate of 10 K min⁻¹. c,d) Development of relative crystallinity with temperature (c) and time (d) for T-C₁₀. The sample was cooled down at a fixed rate of 10 K min⁻¹ and heated at five different rates. e,f) Double-logarithmic linearized Avrami plots (e) and Mo plots (f) of T-C₁₀ during the nonisothermal cold crystallization process.

Information) with respect to the heating rate, the activation energy of the nonisothermal crystallization can be estimated by applying the classical Kissinger equation:

$$\ln\left(\frac{\lambda}{T_p^2}\right) = -\frac{E_a}{RT_p} + C \quad (1)$$

where R is the universal gas constant, T_p is the crystallization peak temperature, λ is the heating rate, E_a is the relevant crystallization activation energy and C is a constant. The slope of plots for $\ln(\lambda/T_p^2)$ versus T_p^{-1} gave (Figure S24, Supporting Information) the value of $-E_a/R$, from which an energy of activation (E_a) of ≈ 65.3 kJ mol $^{-1}$ was calculated.

In order to gain more insight into the crystallization of T-C $_{10}$, a nonisothermal crystallization kinetic study was carried out^[84–87] in a manner similar to that employed with polymers. The relative crystallinity (X_T or X_t), as a function of the crystallization temperature (T) and time (t), is shown in Figure 3c,d and defined as

$$X_T = \frac{\int_{T_0}^T \left(\frac{dH_c}{dT}\right) dT}{\int_{T_0}^{T_\infty} \left(\frac{dH_c}{dT}\right) dT} \quad (2)$$

and

$$X_t = \frac{\int_{t_0}^t \left(\frac{dH_c}{dt}\right) dt}{\int_{t_0}^{t_\infty} \left(\frac{dH_c}{dt}\right) dt} \quad (3)$$

where T_0 (or t_0) and T_∞ (or t_∞) represent the temperature (or time) at the onset and at the end of the crystallization process, respectively. The curves move (Figure 3c) to higher temperatures on increasing the heating rate. In addition, all the curves showed sigmoidal shapes, indicating a fast primary crystallization during the early stages of heating and a slow secondary crystallization in the later stages of heating. Figure 3d, which presents a plot of the relationship between relative crystallinity and crystallization time, shows that a longer time is required for the complete crystallization of T-C $_{10}$ as the rate of heating decreases.

Next, the Avrami equation^[88] was applied in an attempt to investigate the nonisothermal crystallization kinetics, assuming that the relative degree of crystallinity increases with the crystallization time t ,

$$X_t = 1 - \exp(-Z_t t^n) \quad (4)$$

where n is the Avrami crystallization exponent, indicating the nature of nucleation and growth of crystals and Z_t is the crystallization rate parameter. As for the nonisothermal character of the process investigated, the value of Z_t from the above equation should be adequately corrected considering the heating

rate (λ), thus the nonisothermal crystallization parameter (Z_c) is given^[89] as

$$\lg Z_c = \frac{\lg Z_t}{\lambda} \quad (5)$$

Then, the double logarithmic form of Equation (4) can be written as

$$\lg[-\ln(1 - X_t)] = \lg Z_t + n \lg t \quad (6)$$

By plotting (Figure 3e) $\lg[-\ln(1 - X_t)]$ versus $\lg t$ using various heating rates, the values of n can be obtained by linear fitting. Five almost-parallel straight fitting lines were obtained with an adjusted R^2 of more than 0.99, suggesting that the Avrami method could be employed to describe the nonisothermal crystallization of T-C $_{10}$. We found (Table S3 and Figure S25, Supporting Information) that the average values of Avrami exponent (n) were around 4 even under different rates of heating, suggesting that the temperature-triggered assembly mechanism remains unchanged with heating rates. Although in nonisothermal crystallization kinetics, the parameter n does not have the same physical significance as it does in isothermal crystallization kinetics, it could also provide further insight into the process related to 3D crystallization growth and homogeneous nucleation mechanisms.

2.4. Single-Crystal (Super)Structures

In order to present a (super)structural basis for the assembly of the organic semiconductors—namely, C-3 and T-C $_{10}$ —and also provide detailed interactional information within different moieties in the solid state, we investigated the single-crystal (super)structures of both the control compound C-3 and the target compound T-C $_{10}$. Both these compounds assemble into several-hundred-micrometer-long crystals by slowly evaporating the mixed CH $_2$ Cl $_2$ /EtOH solution. From their solid-state (super)structures, we observed many similarities. The distance from silicon to the carbon end is ≈ 26.0 Å (Figure 4a) in C-3 and ≈ 26.1 Å (Figure 4f) in T-C $_{10}$, respectively. We note (Figure 4b,g) that the backbones—from the Si atom to the end of the alkyl chain in the molecule—are almost coplanar. Differences occur in the superstructures when only [C-H $\cdots\pi$] interactions exist (Figure 4c) in the dimer of C-3, while in T-C $_{10}$, it is [$\pi\cdots\pi$] interactions between the adjacent BTBT units that hold the dimers together with a stacking distance of 3.5 Å. The intermolecular interactions of the dimers can be quantified (Figure S18, Supporting Information) using^[90,91] Hirshfeld surface analysis.

In the solid-state superstructure of C-3 in Figure 4d, there are no [$\pi\cdots\pi$] interactions, either between the BTBT π -cores or within the phenyl rings in the docker. The dominant interactions (Figure 4e) are [C-H $\cdots\pi$] and [C-H \cdots S] ones in C-3, which can hardly lock the conformations during the heating process—that is, the structural origin of the several endothermic and exothermic peaks in its DSC heating curves (Figure S21b, Supporting Information) for C-3. By contrast, the solid-state superstructure of T-C $_{10}$ reveals (Figure 4i)

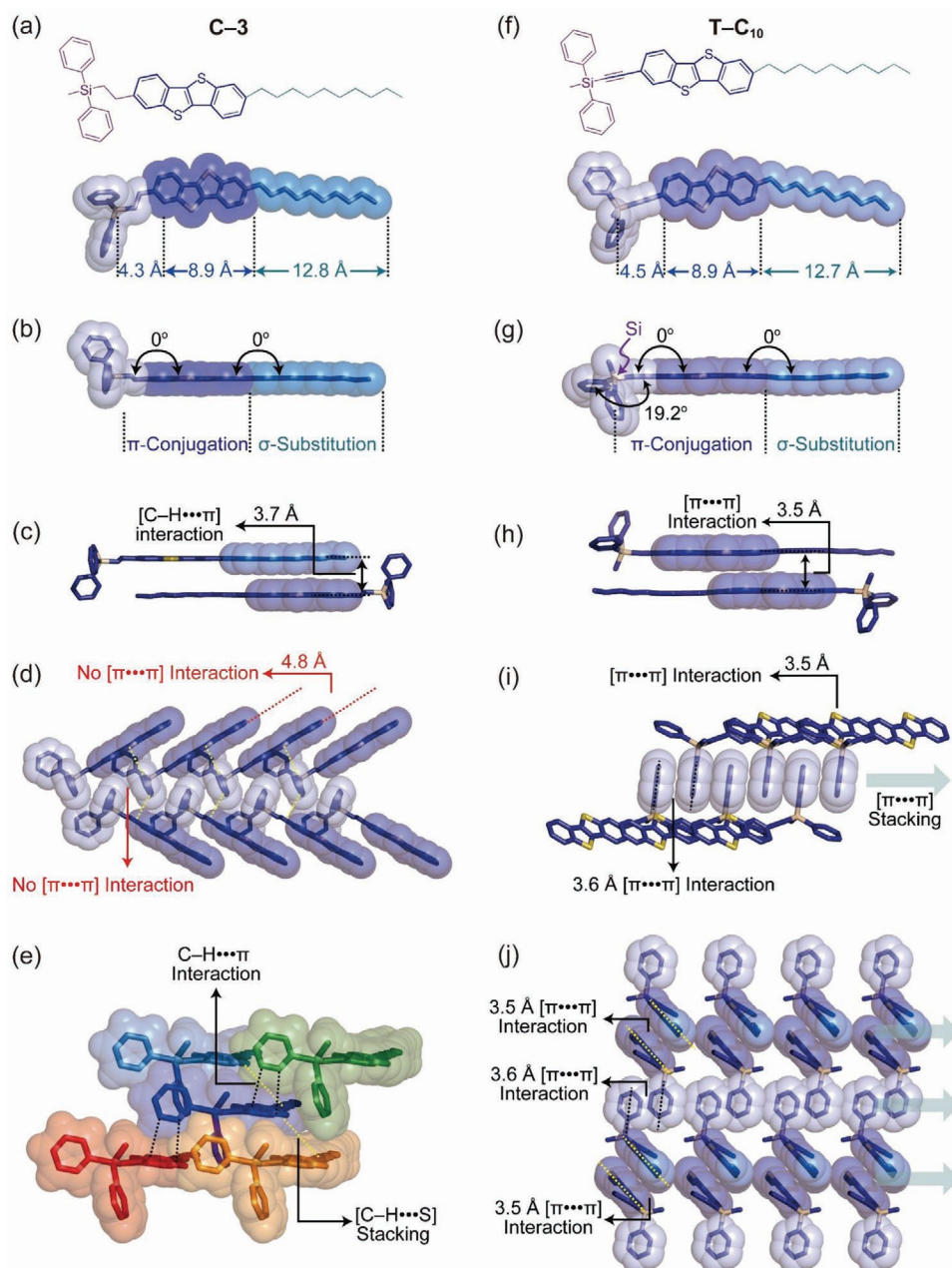


Figure 4. Solid-state X-ray (super)structures of C-3 and T-C₁₀ revealing the (super)structural basis for the temperature-triggered supramolecular assembly mechanism. a) The structural formula and side-on view in the space-filling representation of C-3, showing the torsion associated with the carbon-carbon single bond bridge. b,c) Edge-on view of a space-filling representation, showing the planar conformation of the backbone of C-3 (b) and the face-to-face stacking of two C-3 molecules sustained by [C-H... π] interactions (c). d) Solid-state superstructure of C-3 revealing no [π ... π] interactions involving the phenylene rings in diphenylsilyl dockers and the BTBT π -cores. e) Solid-state superstructure of C-3, revealing a layered structure involving two kinds of weak interactions, namely, [C-H... π] and [C-H...S]. f) Structural formula and side-on view in space-filling representation showing the distances defining the almost linear geometry of T-C₁₀. g,h) Edge-on view of space-filling representations showing the coplanar conformation of the backbone (g) and the face-to-face stacking between adjacent T-C₁₀ molecules sustained by [π ... π] interactions (h). i,j) Solid-state superstructures revealing layers of T-C₁₀ involving two kinds of [π ... π] interactions—namely, [π ... π] interactions involving phenylene rings in the diphenylsilyl dockers and [π ... π] interactions between BTBT π -cores. Hydrogen atoms and solvent molecules are omitted for the sake of clarity.

layered stacks, which differ markedly from the packing structure adopted (Figure 4d) by C-3. This 1D superstructure reveals (Figure 4i) an alignment of the molecules along the stacking direction of phenylene rings in the docker, involving two kinds of [π ... π] interactions—namely, i) [π ... π] interactions between

the phenylene rings in the docker and ii) [π ... π] interactions between the BTBT π -cores. Because of these two cooperative interactions, the molecules are locked in inactive co-conformations. The 3D superstructure (Figure 4j) is a result of a two-level assembly process, i.e., i) one involving adjacent layers sustained

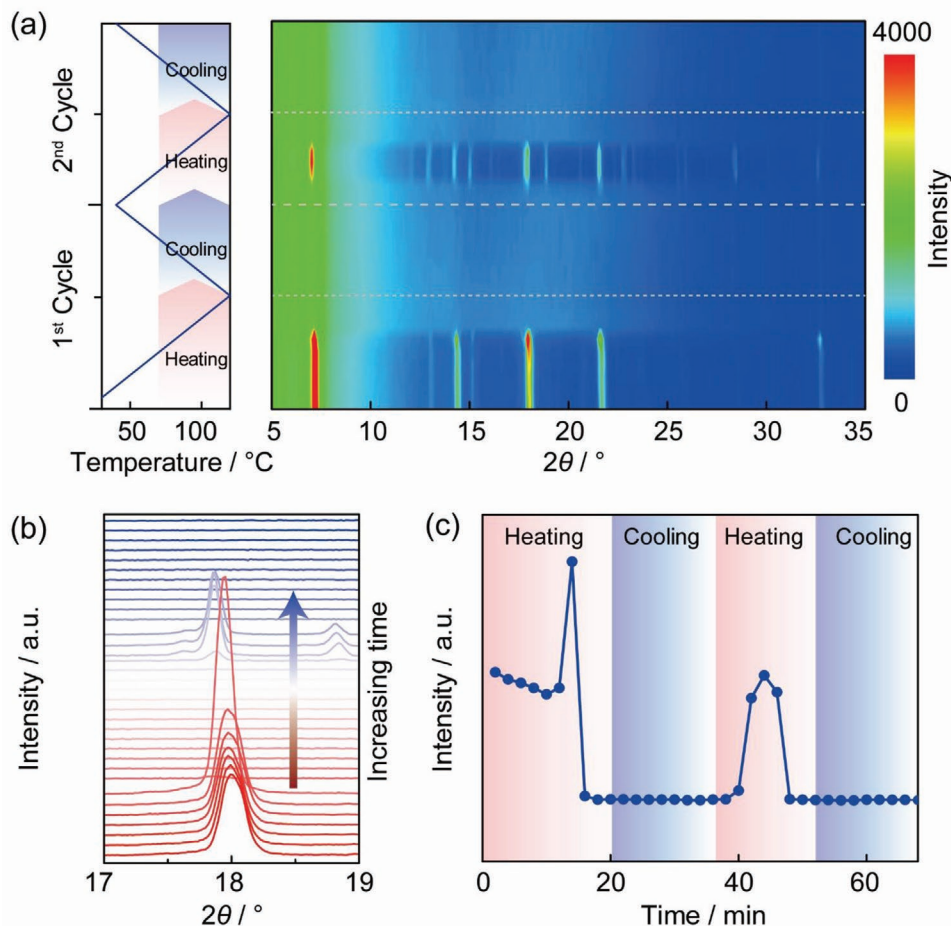


Figure 5. VT-XRD measurements revealing the temperature-triggered assembly of T-C₁₀. a) 2D peak intensities associated with XRD patterns showing the supramolecular assembly process. Left inset: Two programmed heating/cooling cycles. b) 1D peak (at $\approx 18^\circ$) intensities extracted at different temperatures. c) The values of peak intensities extracted from the diffraction peak at $\approx 18^\circ$ against time which can be divided into two heating/cooling cycles (Heating: light red; Cooling: light blue).

by $[\pi \cdot \cdot \cdot \pi]$ interactions between pairs of BTBT units with plane-to-plane separations of 3.5 Å and ii) additional interlamellar assembly supported by $[\pi \cdot \cdot \cdot \pi]$ interactions with plane-to-plane separations of 3.6 Å between phenylene rings in the bulky dockers.

2.5. Variable-Temperature X-ray Diffraction (VT-XRD) Experiments

In order to investigate the influence of temperature on the crystalline behavior of solid-state films on silicon substrates, we performed (Figure 5) in situ variable-temperature X-ray diffraction (VT-XRD) experiments. They were performed on a thin film, spin-coated from 1 mg mL⁻¹ T-C₁₀ CHCl₃ solution. Each XRD curve was recorded in the 2θ region of 5–35° for every 30 min at a scan rate of 0.5° min⁻¹ with a 50 s retention interval between the measurements. Two heating/cooling cycles showed (Figure 5a) distinct diffraction intensity changes, revealing the presence of amorphous-to-crystalline transitions during the heating process. In the first cycle, when T-C₁₀

was heated above its melting point (96.2 ± 0.4 °C), the diffraction peaks disappeared, indicating that the solid-state films of T-C₁₀ turned into isotropic liquids. The sample maintained its glassy state with no diffraction peaks observed during the subsequent cooling process (120 to 40 °C). During the subsequent heating process, however, the missing diffraction peaks showed up (Figure 5a, second cycle) again when starting at ≈ 60 °C and ending at ≈ 90 °C. More significantly, after heating, the crystalline sample exhibited more reflection peaks, indicating a higher crystallinity than that present in the initial state. By extracting (Figure 5b) the peak intensity evolution at $\approx 18.0^\circ$, the assembly trajectories could be divided into (Figure 5c) four stages and two cycles, in good agreement with the DSC results (Figure S20, Supporting Information).

In an attempt to identify the detailed nucleation mechanism of the temperature-triggered supramolecular assembly, we performed atomic force microscopy (AFM) investigations on sub-monolayer films. We collected sequential AFM images in situ and observed the evolution of film morphologies during the pre-nucleation periods. Real-time in situ AFM experiments revealed (Figures S27 and 28, Supporting Information) a two-step

nucleation mechanism for the supramolecular assembly process. First, the evolution of the shape of the as-spin-coated films during the early stage of their assembly demonstrated (Figure S27, Supporting Information) that the amorphous films are not stable and tend to “dissolve” during prolonged growth. In the meantime, some thick clusters grew quickly and eventually overwhelmed the thin domains. In a second step, the thick clusters continued to dissolve (Figure S28, Supporting Information), becoming a source of mass to grow the longer wires. The two-step dissolve-and-grow mechanism resembles an Ostwald ripening process in which stepwise crystallization takes place such that thermodynamically unstable phases often occur first, followed by thermodynamically stable ones. Finally, the amorphous film crystallized (Figure S29, Supporting Information) into ultralong, high-density, and highly ordered microwire arrays.

2.6. Electrical Performance

UV-Vis spectra of the T-C₁₀ thin film deposited on a quartz substrate demonstrated (Figure S17a and Table S1, Supporting Information) apparent redshifted absorption bands relative to those in the solution (CHCl₃) spectrum, indicating strong intermolecular interactions in the thin film. The optical bandgap of T-C₁₀ in CHCl₃ solution and in thin films is estimated to be ≈3.39 (solution) and ≈3.31 (thin films) eV, values which are smaller than that (≈3.65 eV) of C-3 (Figure S17c, Supporting Information), indicating an extension of π -conjugation on account of the presence of the carbon-carbon triple bond in the molecule. After annealing (Figure S17b, Supporting Information), the UV-Vis spectra of T-C₁₀ were redshifted and

broadened, suggesting that there is stronger intermolecular excitonic coupling between neighboring T-C₁₀ molecules, as observed^[78] in crystalline oligothiophene derivatives.

We have fabricated (Figure 6a) organic field-effect transistors (OFETs) based on single-crystalline microwires of T-C₁₀, employing (Figure 6b) a shadow mask technique to deposit the source/drain electrodes. By controlling the concentration of the organic semiconductor solutions, spin-coating speeds, annealing temperatures, and growth times, we are able to obtain isolated and long microwires—surrounded by fractional thin films—on SiO₂ surfaces. By employing a TEM copper grid as a shadow mask, symmetric electrodes can be obtained by thermal evaporation under vacuum. Plots of typical output and transfer curves for an OFET—with a channel length of 90 μm and a channel width of 6 μm —are illustrated in Figure 6c,d. The devices showed electrical responses upon changes in the gate voltages. The highest hole mobilities were calculated (Figure 6e) to be 1.2 $\text{cm}^2 \text{V}^{-1} \text{s}^{-1}$ with an on/off ratio exceeding 10⁵ without any further optimization. This OFET performance is amongst the highest recorded (Table S5, Supporting Information) for 1D organic nanofiber transistors.

The sharpness of the peak (Figure 6e) in the gate-dependent mobility plot indicates^[92] a Schottky contact at the electrode/semiconductor interface. The contact problem occurs during the deposition of the gold electrodes if the temperature of the substrate becomes higher than 100 °C on account of thermal irradiation. The crystals melt at this temperature. After optimizing the thermal evaporation process by cooling the substrate, the evaporated gold nanoclusters can also cause damage to the microwire in the contact area, leaving it disordered and leading to high contact resistance. Ultimately, the contact issue leads (Figure 6c,d) to instability at high bias and gate voltages.

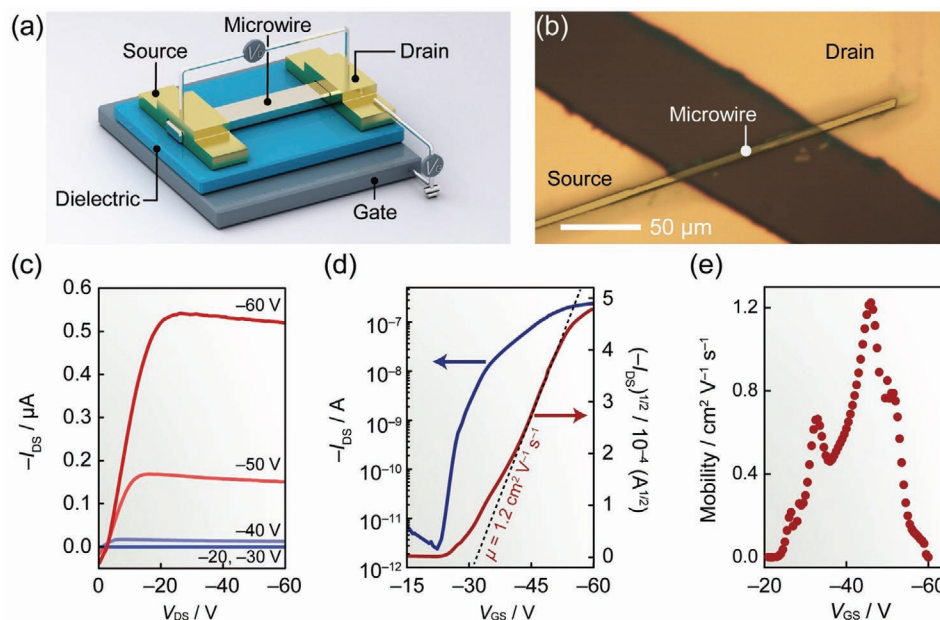


Figure 6. OFET performance of the single-crystalline microwire of T-C₁₀. a,b) Schematic illustration (a) and optical image (b) showing a OFET device with a bottom-gated top-contact configuration. c) Output characteristics of the OFET. The gate voltage (V_{GS}) ranges from 0 to -60 V in -10 V steps. d) Transfer characteristics with the source–drain voltage (V_{DS}) = -60 V. e) Gate voltage dependence of the field-effect mobility obtained from the local slope in the $I_{\text{DS}}^{1/2}$ - V_{GS} curve shown in (d).

We intend to explore this device fabrication method with improved OFET properties, based on assembled microwire arrays, in our future research.

3. Conclusion

Temperature-triggered supramolecular assembly takes advantage of a process for fabricating highly ordered organic semiconductor arrays. We have demonstrated that, in contrast with previous static self-assembly processes occurring in solution, the Tetris strategy makes use of the dynamic characteristics of noncovalent bonding interactions in order to heal the disorders and defects at a supramolecular level. In order to gain a detailed understanding of this assembly process, we have employed thermal and single-crystal (super)structure analyses to reveal a bigger picture of the structural origin of the supramolecular assembly process—namely, the rotation around the triple bond bridge occurs upon heating, leading to i) a change in the orientation of the docker pointing either up or down, thereby ii) inducing conformation-fitting upon adjacent molecules through two kinds of intermolecular [$\pi \cdots \pi$] interactions, and finally iii) locking the nearby molecules into inactive conformations. The single-crystalline microwires exhibit hole-mobility with average values of $\approx 1.0 \text{ cm}^2 \text{ V}^{-1} \text{ s}^{-1}$. The ease of solution processing, the temperature-triggered supramolecular assembly, and the resulting highly ordered organic semiconductor arrays illustrate how self-assembly represents an extraordinarily useful approach for the manufacture of the next generation of smart materials.

Supporting Information

Supporting Information is available from the Wiley Online Library or from the author.

Acknowledgements

H.C. and W.Z. contributed equally to the work. The authors thank Northwestern University (NU) for their continued support of this research. This work made use of the IMSERC X-ray facility at NU, which has received support from the Soft and Hybrid Nanotechnology Experimental (SHyNE) Resource (NSF ECCS-1542205), and NU. The research at Peking University was supported by the National Key R&D Program of China (2017YFA0204901) and the National Natural Science Foundation of China (21727806 and 21933001). X.G. acknowledges the Tencent Foundation through the XPLOER PRIZE. Tetris is a registered trademark of Tetris Holding, LLC, used with permission.

Conflict of Interest

The authors declare no conflict of interest.

Data Availability Statement

The data that support the findings of this study are available from the corresponding author upon reasonable request.

Keywords

[$\pi \cdots \pi$] interactions, cold crystallization, noncovalent bonding interactions, organic field-effect transistors, semiconductors, solution processability

Received: February 22, 2021

Revised: April 19, 2021

Published online: July 11, 2021

- [1] T. F. A. De Greef, M. M. J. Smulders, M. Wolfs, A. P. H. J. Schenning, R. P. Sijbesma, E. W. Meijer, *Chem. Rev.* **2009**, *109*, 5687.
- [2] Z. J. Chen, A. Lohr, C. R. Saha-Möllner, F. Würthner, *Chem. Soc. Rev.* **2009**, *38*, 564.
- [3] T. Aida, E. W. Meijer, S. I. Stupp, *Science* **2012**, *335*, 813.
- [4] P. Xing, Y. Zhao, *Acc. Chem. Res.* **2018**, *51*, 2324.
- [5] F. J. M. Hoeben, P. Jonkheijm, E. W. Meijer, A. P. H. J. Schenning, *Chem. Rev.* **2005**, *105*, 1491.
- [6] V. Palermo, P. Samorì, *Angew. Chem., Int. Ed.* **2007**, *46*, 4428.
- [7] A. Saeki, Y. Koizumi, T. Aida, S. Seki, *Acc. Chem. Res.* **2012**, *45*, 1193.
- [8] E. Moulin, J. J. Armao, N. Giuseppone, *Acc. Chem. Res.* **2019**, *52*, 975.
- [9] L. R. MacFarlane, H. Shaikh, J. D. Garcia-Hernandez, M. Vespa, T. Fukui, I. Manners, *Nat. Mater. Rev.* **2021**, *6*, 7.
- [10] Y. Yao, L. Zhang, E. Orgiu, P. Samorì, *Adv. Mater.* **2019**, *31*, 1900599.
- [11] A. P. H. J. Schenning, E. W. Meijer, *Chem. Commun.* **2005**, 3245.
- [12] A. Jain, S. J. George, *Mater. Today* **2015**, *18*, 206.
- [13] E. Moulin, J.-J. Cid, N. Giuseppone, *Adv. Mater.* **2013**, *25*, 477.
- [14] E. W. Meijer, A. P. H. J. Schenning, *Nature* **2002**, *419*, 353.
- [15] D. He, Y. Zhang, Q. Wu, R. Xu, H. Nan, J. Liu, J. Yao, Z. Wang, S. Yuan, Y. Li, Y. Shi, J. Wang, Z. Ni, L. He, F. Miao, F. Song, H. Xu, K. Watanabe, T. Taniguchi, J.-B. Xu, X. Wang, *Nat. Commun.* **2014**, *5*, 5162.
- [16] D. González-Rodríguez, A. P. H. J. Schenning, *Chem. Mater.* **2011**, *23*, 310.
- [17] W. Zhao, B. Qiao, J. Tropp, M. Pink, J. D. Azoulay, A. H. Flood, *J. Am. Chem. Soc.* **2019**, *141*, 4980.
- [18] P. Xing, Y. Li, S. Xue, S. Z. F. Phua, C. Ding, H. Chen, Y. Zhao, *J. Am. Chem. Soc.* **2019**, *141*, 9946.
- [19] R. Gutzler, C. Fu, A. Dadvand, Y. Hua, J. M. MacLeod, F. Rosei, D. F. Perepichka, *Nanoscale* **2012**, *4*, 5965.
- [20] L. Bai, P. Bose, Q. Gao, Y. Li, R. Ganguly, Y. Zhao, *J. Am. Chem. Soc.* **2017**, *139*, 436.
- [21] X.-H. Ding, Y.-Z. Chang, C.-J. Ou, J.-Y. Lin, L.-H. Xie, W. Huang, *Natl. Sci. Rev.* **2020**, *7*, 1906.
- [22] J. P. Hill, W. S. Jin, A. Kosaka, T. Fukushima, H. Ichihara, T. Shimomura, K. Ito, T. Hashizume, N. Ishii, T. Aida, *Science* **2004**, *304*, 1481.
- [23] J. F. Neal, W. Zhao, A. J. Grooms, M. A. Smeltzer, B. M. Shook, A. H. Flood, H. C. Allen, *J. Am. Chem. Soc.* **2019**, *141*, 7876.
- [24] T. Fukui, J. D. Garcia-Hernandez, L. R. MacFarlane, S. Lei, G. R. Whittell, I. Manners, *J. Am. Chem. Soc.* **2020**, *142*, 15038.
- [25] H. Qiu, Z. M. Hudson, M. A. Winnik, I. Manners, *Science* **2015**, *347*, 1329.
- [26] C. R. Benson, L. Kacenauskaite, K. L. VanDenburgh, W. Zhao, B. Qiao, T. Sadhukhan, M. Pink, J. Chen, S. Borgi, C.-H. Chen, B. J. Davis, Y. C. Simon, K. Raghavachari, B. W. Laursen, A. H. Flood, *Chem* **2020**, *6*, 1978.
- [27] B. Qiao, B. E. Hirsch, S. Lee, M. Pink, C.-H. Chen, B. W. Laursen, A. H. Flood, *J. Am. Chem. Soc.* **2017**, *139*, 6226.
- [28] A. Das, S. Ghosh, *Angew. Chem., Int. Ed.* **2014**, *53*, 2038.
- [29] W. Zhu, R. Zheng, Y. Zhen, Z. Yu, H. Dong, H. Fu, Q. Shi, W. Hu, *J. Am. Chem. Soc.* **2015**, *137*, 11038.

- [30] H. Shaikh, X.-H. Jin, R. L. Harniman, R. M. Richardson, G. R. Whittell, I. Manners, *J. Am. Chem. Soc.* **2020**, *142*, 13469.
- [31] V. Percec, M. Glodde, T. K. Bera, Y. Miura, I. Shiyonovskaya, K. D. Singer, V. S. K. Balagurusamy, P. A. Heiney, I. Schnell, A. Rapp, H. W. Spiess, S. D. Hudson, H. Duan, *Nature* **2002**, *419*, 384.
- [32] S. S. Babu, S. Prasanthkumar, A. Ajayaghosh, *Angew. Chem., Int. Ed.* **2012**, *51*, 1766.
- [33] S. S. Babu, V. K. Praveen, A. Ajayaghosh, *Chem. Rev.* **2014**, *114*, 1973.
- [34] A. Goujon, G. Mariani, T. Lang, E. Moulin, M. Rawiso, E. Buhler, N. Giuseppone, *J. Am. Chem. Soc.* **2017**, *139*, 4923.
- [35] G. Liu, C. Zhou, W. L. Teo, C. Qian, Y. Zhao, *Angew. Chem., Int. Ed.* **2019**, *58*, 9366.
- [36] C. Rest, R. Kandaneli, G. Fernández, *Chem. Soc. Rev.* **2015**, *44*, 2543.
- [37] S. Yagai, Y. Monma, N. Kawauchi, T. Karatsu, A. Kitamura, *Org. Lett.* **2007**, *9*, 1137.
- [38] L. Welte, A. Calzolari, R. Di Felice, F. Zamora, J. Gomez-Herrero, *Nat. Nanotechnol.* **2010**, *5*, 110.
- [39] Y. Yamamoto, T. Fukushima, Y. Suna, N. Ishii, A. Saeki, S. Seki, S. Tagawa, M. Taniguchi, T. Kawai, T. Aida, *Science* **2006**, *314*, 1761.
- [40] D. Wu, L. Zhi, G. J. Bodwell, G. Cui, N. Tsao, K. Müllen, *Angew. Chem., Int. Ed.* **2007**, *46*, 5417.
- [41] L. Zhang, X. Zhong, E. Pavlica, S. Li, A. Klekachev, G. Bratina, T. W. Ebbesen, E. Orgiu, P. Samorì, *Nat. Nanotechnol.* **2016**, *11*, 900.
- [42] W. Zhang, W. Jin, T. Fukushima, A. Saeki, S. Seki, T. Aida, *Science* **2011**, *334*, 340.
- [43] F. Würthner, Z. Chen, F. J. M. Hoeben, P. Osswald, C.-C. You, P. Jonkheijm, J. v. Herrikhuysen, A. P. H. J. Schenning, P. P. A. M. van der Schoot, E. W. Meijer, E. H. A. Beckers, S. C. J. Meskers, R. A. J. Janssen, *J. Am. Chem. Soc.* **2004**, *126*, 10611.
- [44] N. Sakai, R. Bhosale, D. Emery, J. Mareda, S. Matile, *J. Am. Chem. Soc.* **2010**, *132*, 6923.
- [45] L. Jiang, H. Dong, Q. Meng, H. Li, M. He, Z. Wei, Y. He, W. Hu, *Adv. Mater.* **2011**, *23*, 2059.
- [46] Y. Shi, L. Jiang, J. Liu, Z. Tu, Y. Hu, Q. Wu, Y. Yi, E. Gann, C. R. McNeill, H. Li, W. Hu, D. Zhu, H. Siringhaus, *Nat. Commun.* **2018**, *9*, 2933.
- [47] H. Chen, S. Dong, M. Bai, N. Cheng, H. Wang, M. Li, H. Du, S. Hu, Y. Yang, T. Yang, F. Zhang, L. Gu, S. Meng, S. Hou, X. Guo, *Adv. Mater.* **2015**, *27*, 2113.
- [48] Q. Wang, F. Yang, Y. Zhang, M. Chen, X. Zhang, S. Lei, R. Li, W. Hu, *J. Am. Chem. Soc.* **2018**, *140*, 5339.
- [49] X. Zhang, C.-H. Hsu, X. Ren, Y. Gu, B. Song, H.-J. Sun, S. Yang, E. Chen, Y. Tu, X. Li, X. Yang, Y. Li, X. Zhu, *Angew. Chem., Int. Ed.* **2015**, *54*, 114.
- [50] N. Seiki, Y. Shoji, T. Kajitani, F. Ishiwari, A. Kosaka, T. Hikima, M. Takata, T. Someya, T. Fukushima, *Science* **2015**, *348*, 1122.
- [51] F. Yang, S. Cheng, X. Zhang, X. Ren, R. Li, H. Dong, W. Hu, *Adv. Mater.* **2018**, *30*, 1702415.
- [52] T. Yokota, T. Kajitani, R. Shidachi, T. Tokuhara, M. Kaltenbrunner, Y. Shoji, F. Ishiwari, T. Sekitani, T. Fukushima, T. Someya, *Nat. Nanotechnol.* **2018**, *13*, 139.
- [53] J. R. Dobscha, H. D. Castillo, Y. Li, R. E. Fadler, R. D. Taylor, A. A. Brown, C. Q. Trainor, S. L. Tait, A. H. Flood, *J. Am. Chem. Soc.* **2019**, *141*, 17588.
- [54] L. Sun, Y. Wang, F. Yang, X. Zhang, W. Hu, *Adv. Mater.* **2019**, *31*, 1902328.
- [55] H. Jiang, W. Hu, *Angew. Chem., Int. Ed.* **2020**, *59*, 1408.
- [56] Y. Wang, L. Sun, C. Wang, F. Yang, X. Ren, X. Zhang, H. Dong, W. Hu, *Chem. Soc. Rev.* **2019**, *48*, 1492.
- [57] X.-H. Jin, M. B. Price, J. R. Finnegan, C. E. Boot, J. M. Richter, A. Rao, S. M. Menke, R. H. Friend, G. R. Whittell, I. Manners, *Science* **2018**, *360*, 897.
- [58] D. Bochicchio, M. Salvalaglio, G. M. Pavan, *Nat. Commun.* **2017**, *8*, 147.
- [59] D. Bochicchio, S. Kwangmettata, T. Kudernac, G. M. Pavan, *ACS Nano* **2019**, *13*, 4322.
- [60] P. Gasparotto, D. Bochicchio, M. Ceriotti, G. M. Pavan, *J. Phys. Chem. B* **2020**, *124*, 589.
- [61] S. Rieth, C. Baddeley, J. D. Badjić, *Soft Matter* **2007**, *3*, 137.
- [62] X. Wang, G. Guerin, H. Wang, Y. Wang, I. Manners, M. A. Winnik, *Science* **2007**, *317*, 644.
- [63] H. Qiu, Z. M. Hudson, M. A. Winnik, I. Manners, *Science* **2015**, *347*, 1329.
- [64] L. Tauk, A. P. Schröder, G. Decher, N. Giuseppone, *Nat. Chem.* **2009**, *1*, 649.
- [65] E. Moulin, F. Niess, M. Maaloum, E. Buhler, I. Nyrkova, N. Giuseppone, *Angew. Chem., Int. Ed.* **2010**, *49*, 6974.
- [66] V. Faramarzi, F. Niess, E. Moulin, M. Maaloum, J.-F. Dayen, J.-B. Beaufrand, S. Zanetini, B. Doudin, N. Giuseppone, *Nat. Chem.* **2012**, *4*, 485.
- [67] Z. Zhang, L. Cheng, J. Zhao, H. Zhang, X. Zhao, Y. Liu, R. Bai, H. Pan, W. Yu, X. Yan, *J. Am. Chem. Soc.* **2021**, *143*, 902.
- [68] E. Moulin, F. Niess, M. Maaloum, E. Buhler, I. Nyrkova, N. Giuseppone, *Angew. Chem., Int. Ed.* **2010**, *49*, 6974.
- [69] G. Liu, J. Sheng, W. L. Teo, G. Yang, H. Wu, Y. Li, Y. Zhao, *J. Am. Chem. Soc.* **2018**, *140*, 16275.
- [70] A. Osypenko, E. Moulin, O. Gavati, G. Fuks, M. Maaloum, M. A. J. Koenis, W. J. Buma, N. Giuseppone, *Chem. - Eur. J.* **2019**, *25*, 13008.
- [71] R. D. Mukhopadhyay, A. Ajayaghosh, *Science* **2015**, *349*, 241.
- [72] H. Iino, T. Usui, J.-I. Hanna, *Nat. Commun.* **2015**, *6*, 6828.
- [73] H. Ebata, T. Izawa, E. Miyazaki, K. Takimiya, M. Ikeda, H. Kuwabara, T. Yui, *J. Am. Chem. Soc.* **2007**, *129*, 15732.
- [74] J. Mei, Y. Diao, A. L. Appleton, L. Fang, Z. Bao, *J. Am. Chem. Soc.* **2013**, *135*, 6724.
- [75] K. Takimiya, S. Shinamura, I. Osaka, E. Miyazaki, *Adv. Mater.* **2011**, *23*, 4347.
- [76] C. Wang, H. Dong, W. Hu, Y. Liu, D. Zhu, *Chem. Rev.* **2012**, *112*, 2208.
- [77] K. Takimiya, I. Osaka, T. Mori, M. Nakano, *Acc. Chem. Res.* **2014**, *47*, 1493.
- [78] S. Dong, H. Zhang, L. Yang, M. Bai, Y. Yao, H. Chen, L. Gan, T. Yang, H. Jiang, S. Hou, L. Wan, X. Guo, *Adv. Mater.* **2012**, *24*, 5576.
- [79] J. Mei, Z. Bao, *Chem. Mater.* **2014**, *26*, 604.
- [80] B. Košata, J. Svoboda, V. Novotná, M. Glogarová, *Liq. Cryst.* **2004**, *31*, 1367.
- [81] H. Chen, M. Li, Z. Lu, X. Wang, J. Yang, Z. Wang, F. Zhang, C. Gu, W. Zhang, Y. Sun, J. Sun, W. Zhu, X. Guo, *Nat. Commun.* **2019**, *10*, 3872.
- [82] A. Klapars, S. L. Buchwald, *J. Am. Chem. Soc.* **2002**, *124*, 14844.
- [83] J. Xin, X. Meng, X. Xu, Q. Zhu, H. B. Naveed, W. Ma, *Matter* **2019**, *1*, 1316.
- [84] S. W. Lee, M. Ree, C. E. Park, Y. K. Jung, C. S. Park, Y. S. Jin, D. C. Bae, *Polymer* **1999**, *40*, 7137.
- [85] W. Xu, M. Ge, P. He, *J. Polym. Sci., Part B: Polym. Phys.* **2002**, *40*, 408.
- [86] S. P. Lonkar, S. Morlat-Therias, N. Caperaa, F. Leroux, J. L. Gardette, R. P. Singh, *Polymer* **2009**, *50*, 1505.
- [87] F. Lu, H. Yu, C. Yan, J. Yao, *RSC Adv.* **2016**, *6*, 46008.
- [88] M. Avrami, *J. Chem. Phys.* **1940**, *8*, 212.
- [89] A. Jeziorny, *Polymer* **1978**, *19*, 1142.
- [90] M. A. Spackman, D. Jayatilaka, *CrystEngComm* **2009**, *11*, 19.
- [91] J. J. McKinnon, D. Jayatilaka, M. A. Spackman, *Chem. Commun.* **2007**, 3814.
- [92] R. Versluis, S. Poletto, N. Khammassi, B. Tarasinski, N. Haider, D. J. Michalak, A. Bruno, K. Bertels, L. DiCarlo, *Phys. Rev. Appl.* **2017**, *8*, 034021.